ARTICLE

A case study for the formation of stanene on a metal surface

M. Maniraj[1], B. Stadtmüller[1,2], D. Jungkenn[1], M. Düvel[3], S. Emmerich[1,2], W. Shi[4,5], J. Stöckl[1], L. Lyu[1], J. Kollamana[1], Z. Wei[1], A. Jurenkow[1], S. Jakobs[1], B. Yan[4], S. Steil[3], M. Cinchetti[6], S. Mathias[3,7] & M. Aeschlimann[1]

The discovery and realization of graphene as an ideal two-dimensional (2D) material has triggered extensive efforts to create similar 2D materials with exciting spin-dependent properties. Here, we report on a novel Sn 2D superstructure on Au(111) that shows similarities and differences to the expected electronic features of ideal stanene. Using spin- and angle-resolved photoemission spectroscopy, we find that a particular Sn/Au superstructure reveals a linearly dispersing band centered at the $\bar{\Gamma}$-point and below the Fermi level with anti-parallel spin polarization and a Fermi velocity of $v_F \approx 1\times10^6$ m/s, the same value as for graphene. We attribute the origin of the band structure to the hybridization between the Sn and the Au orbitals at the 2D Sn-Au interface. Considering that free-standing stanene simply cannot exist, our investigated structure is an important step towards the search of useful stanene-like overstructures for future technological applications.

[1] Department of Physics and Research Center OPTIMAS, University of Kaiserslautern, 67663 Kaiserslautern, Germany. [2] Graduate School of Excellence Materials Science in Mainz, Erwin-Schrödinger-Straβe 46, 67663 Kaiserslautern, Germany. [3] I. Physikalisches Institut, Georg-August-Universität Göttingen, Friedrich-Hund-Platz 1, 37077 Göttingen, Germany. [4] Max Planck Institute for Chemical Physics of Solids, 01187 Dresden, Germany. [5] School of Physical Science and Technology, Shanghai Tech University, Shanghai 200031, China. [6] Experimentelle Physik VI, Technische Universität Dortmund, 44221 Dortmund, Germany. [7] International Center for Advanced Studies of Energy Conversion (ICASEC), Georg-August-Universität Göttingen, D-37077 Göttingen, Germany. Correspondence and requests for materials should be addressed to M.M. (email: mr.maniraj@gmail.com)

One of the recent milestone discoveries in condensed matter physics is the experimental realization of graphene[1,2]. Graphene is the ultimate two-dimensional (2D) material that consists of a single layer of carbon atoms with sp^2 hybridization arranged in a honeycomb structure. One of the most remarkable properties of graphene is its electronic structure, which has a Dirac cone-like spectrum. The very high mobility of relativistic massless Dirac Fermions in the Dirac cone holds the promise for future technological applications. This accelerated the research on graphene and alternative graphene-like 2D materials. In this direction, a new set of materials has been predicted to be a direct analogy to graphene, for instance, if all carbon atoms in graphene are replaced by either Si, Ge, and Sn, which results in silicene, germanene, and stanene, respectively[3,4]. Since all of these group-IV elements have a similar outer shell electronic configuration but different spin-orbit coupling strengths, they are expected to exhibit the typical characteristic properties of graphene with the addition of spin-dependent phenomena. Out of them, however, only graphene is found to be stable in the free-standing form, whereas all others must be grown on a substrate due to the more favorable sp^3 hybridization. In reality, the formation of a stable graphene-like 2D structure on a given surface is subject to a delicate balance between various adsorbate-adsorbate and adsorbate-substrate interactions, and thus the associated characteristic properties vary widely. Nevertheless, due to the stronger spin-orbit coupling, these novel graphene-like 2D materials can exhibit additional new and intriguing properties, as for instance the quantum spin hall (QSH) effect[5]. Unfortunately, however, available materials with such properties are until now based on complex alloys or multi-component materials with different sublattices, which are challenging to fabricate in terms of large-scale production.

In this regard, and with respect to the potentially easier to fabricate elemental materials stanene, germanene, and silicene, stanene seems the most promising graphene-like 2D material, as it is predicted to be not only a QSH insulator with nontrivial topological properties[5–7], but also shows topological superconductivity[8], enhanced thermoelectricity[9], and valleytronics[10]. A first realization of a stanene-like overlayer has been reported recently[11,12], with the topological insulator Bi_2Te_3 as the supporting substrate. In the search for alternative substrate materials, recent theoretical works predicted many possibilities[6,11,13–16], and one among them is the Au(111) surface[17]. At the same time, Sn and Au are receiving renewed interest due to the discovery of an elemental topological insulator phase in α-Sn[18–20], and the recent reinterpretation of the Shockley surface states on the Au(111) surface as a topologically derived surface state[21]. These aspects motivated us to investigate the formation of 2D Sn superstructures on an Au(111) crystal.

In this article, we provide experimental evidence for the formation of a highly intriguing 2D hexagonal Sn-dimer phase in the manifold of Sn/Au(111) surface reconstructions which exhibits electronic states with similarities to some of the expected properties of a graphene-like 2D material. This particular Sn/Au superstructure reveals a stretched hexagonal lattice with two Sn atoms per unit cell arranged in a dimer-like structure as deduced from our low energy electron diffraction (LEED) and scanning tunneling microscopy (STM) experiments. Interestingly, our spin- and angle-resolved photoemission spectroscopy (ARPES) studies show that the occupied band structure of this superstructure exhibits a linearly dispersing band around the $\bar{\Gamma}$ point of the surface Brillouin zone up to the Fermi-level with a positive slope for negative momenta and negative slope of positive momenta. Both branches of this band reveal a spin-polarization similar in magnitude but opposite in sign, i.e., a spin-texture comparable to the one of a three-dimensional topological

insulator. These intriguing properties are attributed to the lateral interaction between the Sn atoms in the dimer structure in conjunction with the hybridization between Sn and the Au orbitals at the Sn-Au interface. We thus argue that interface hybridization is not always detrimental, but can be actively used to design 2D interface layers with yet largely unexplored spin-dependent electronic properties.

Results

Lateral order of the Sn/Au(111) interface. We start with the growth behavior and the structure identification of the fabricated Sn superstructures on Au(111). Below 1 monolayer (ML) of Sn coverage, Sn shows a variety of superstructures on the Au(111) surface depending on the Sn coverage and the post-deposition annealing temperature. Those superstructures are summarized in the structural phase diagram in Fig. 1. The pristine Au(111) surface shows the well-known $(22 \times \sqrt{3})$ herringbone reconstruction (Fig. 1a). At 0.3 ML of Sn, the herringbone reconstruction vanishes and is replaced by a $(\sqrt{3} \times \sqrt{3})$R30° superstructure, named as $\sqrt{3}$ phase (Fig. 1b). Around 0.6 ML of Sn, a new superstructure appears (Fig. 1c)[22], named as X phase (see Supplementary Figure 1). For higher Sn coverage (up to about 2 ML), the LEED pattern remains identical.

We now focus on the effect of post-deposition annealing on the X-phase obtained for 0.6 ML of Sn on Au(111). This phase exhibits an irreversible structural phase transition that is caused by a thermally driven desorption of Sn adatoms, which depends on the post-deposition annealing temperature, see Fig. 1c–f and Supplementary Movie 1. At room temperature, the X phase is stable, while annealing to about 450 K induces a gradual structural phase transition from the X phase to an intermediate phase. A typical LEED pattern of this phase corresponding to a double-honeycomb-like structure is shown in Fig. 1d. When the temperature is carefully increased further to 455 K, a stretched hexagon structure appears, named as $\sqrt{7}$ phase (discussed below). Finally, when the temperature is raised beyond 470 K, a $\sqrt{3}$ superstructure appears[23]. All these superstructures are stable at room temperature after post-deposition annealing.

Out of the manifold of superstructures observed for Sn/Au(111) shown in the structural phase diagram (Fig. 1), we find that the $\sqrt{7}$ phase exhibits intriguing electronic properties far beyond the expectations of a conventional surface reconstruction. We will hence focus on this phase in the following discussion. Figure 1e shows the LEED pattern of the $\sqrt{7}$ phase superimposed with the positions of simulated diffraction spots (colored dots, each color indicates the set of diffraction spots of one rotational domain, for additional information see Supplementary Figure 2). The best agreement between experiment and simulation was achieved for the structure with the superstructure matrix of $\begin{bmatrix} 2 & -1 \\ 3 & 1 \end{bmatrix}$ (or shortly $\sqrt{7}$ phase) with 2D space group of *c2mm*. Hence, the periodic arrangement of the Sn atoms, i.e., the size and shape of the superstructure unit cell, can be classified as a stretched hexagon (see Supplementary Figure 3) as will be discussed in the following.

In order to determine the position of the Sn atoms within the stretched hexagon lattice, we carried out STM measurements on the $\sqrt{7}$ phase. The large scale STM image (300 nm × 300 nm) in Fig. 2a shows the morphology of the Sn overlayer film. We find smooth and island-free terraces that are separated by atomic steps with a uniform height of 2.3 ± 0.2 Å (Fig. 2b), which is comparable to the step height of Au(111). Hence, the Sn atoms form a homogeneous and atomically flat single layer of Sn on the Au(111) surface, i.e., the overlayer film is uniform over several hundreds of nanometers, even spanning over multiple terraces
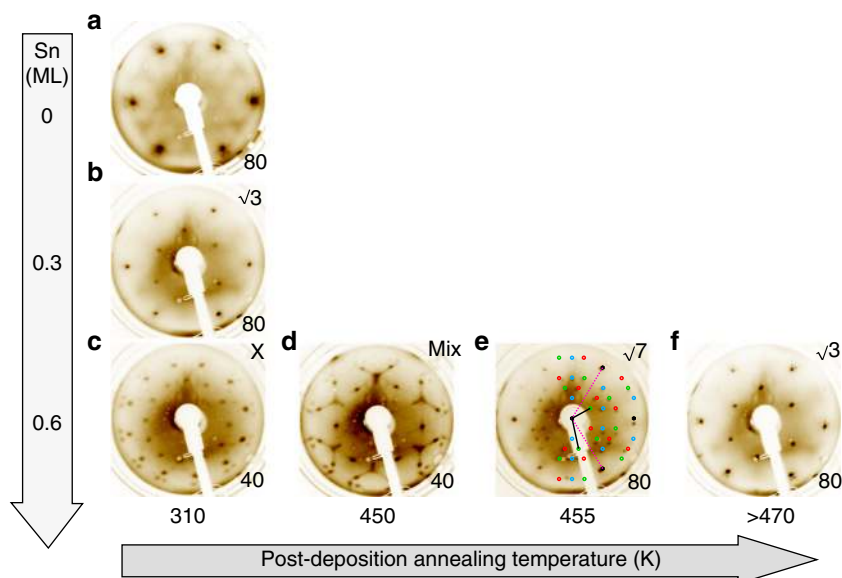
Fig. 1 Structural phase diagram of Sn/Au(111) interface. Low energy electron diffraction (LEED) patterns of a pristine Au(111) surface and of several superstructures of Sn/Au(111) depending on the Sn coverage and post-deposition annealing temperature are shown in **a** and **b**–**f**, respectively. The short names of the superstructures and the electron beam energies in eV are shown in the top-right and bottom-right of all individual images. Sn coverage is provided in monolayer (ML). A simulated LEED pattern of the $\sqrt{7}$ Sn/Au(111) superstructure is superimposed onto the diffraction data in **e** as colored dots. The different colors distinguish the diffraction spots of different structurally equivalent rotational- and mirror domains

and step edges. In particular, the homogeneous growth over step edges underlines the possibility to grow this structure on even larger scales. The detailed atomic arrangement within the unit cell of the superstructure lattice can be obtained from the high-resolution STM image shown in Fig. 2c. The corresponding unit cell of the $\sqrt{7}$ superstructure is marked in pink. In addition, we highlight the stretched hexagon that results from this unit cell in yellow. The atoms forming the unit cell are drawn as spheres on top of the STM data. We find five atoms per unit cell, two with bright contrast forming a dimer-like structure along the <110> direction of the Au(111) surface, and three atomic sites with dark contrast. We assign these bright atoms to Sn, in agreement with previous DFT calculations that predicted the formation of isolated dimers of Sn atoms on Au(111) as a stable configuration for this interface[17]. The dark spots (green circles in Fig. 2c) mark the position of the Au atoms underneath the Sn overlayer. The Sn atoms forming the dimer-like structure are separated by 2.8 Å along the <110> direction, which corresponds to the spacing also observed for Sn gas phase dimers (2.8 Å)[17]. In addition, this value is precisely the surface lattice spacing between two equivalent Au (111) adsorption sites and hence indicates that both dimer atoms occupy identical adsorption sites on the Au surface. This is further supported by a line-scan profile along the <110> direction (Fig. 2d) that additionally reveals a negligible buckling of the dimer adatoms. Based on our structural analysis, we can thus conclude that the $\sqrt{7}$ superstructure shows a stretched hexagon lattice structure with a dimer-like arrangement of two atoms per primitive cell. Based on our experimental findings, we propose a structural model for the $\sqrt{7}$ phase which is shown in Figs 2e, f. The adsorption sites of both Sn atoms could not be determined experimentally. However, in the light of the DFT results by Nigam et al.[17], we propose that both Sn atoms adsorb on identical face centered cubic (fcc) hollow sites. In addition, our structural model is also fully in line with our LEED analysis which is confirmed by the Fast Fourier transform image shown in Fig. 2g (also see Supplementary Figure 2).

Electronic band structure. We now turn to the question in how far this hexagonal dimer Sn structure on Au(111) shows similarities and differences to expected electronic features of graphene-like 2D materials. Figure 3a shows the ARPES intensity map measured along the $\bar{\Gamma}$-$\bar{K}$ high-symmetry direction of the Au(111) surface Brillouin zone. Note that the high surface symmetry (p3m1) of the Au(111) surface results in three rotational domains of the $\sqrt{7}$ superstructure as shown in Supplementary Figure 2 and Supplementary Figure 4. Consequently, the experimental ARPES data recorded along the high-symmetry directions of the Au substrate contain contributions from all three domains. A zoomed-in view of the ARPES intensity map around the $\bar{\Gamma}$ point shown in Fig. 3b indicates the presence of a linearly dispersing band (marked by green lines) near the Fermi level with positive slope for negative momenta and negative slope for positive momenta, labeled as B1 (see Supplementary Figure 5 for a waterfall-plot of the same data). The crossing point of this band B1 is located at the Fermi level ($E_D = 0 \pm 40$ meV), as obtained by extrapolating the linear fits to the data shown in Supplementary Figure 6. From the linear dispersion of this band B1, we can determine the Fermi velocity v_F of the electrons by using $E = \hbar k v_F$. We obtain $v_F \approx 1 \times 10^6$ m/s, the same value as for graphene[24,25]. This unexpectedly high Fermi velocity is even higher than the value predicted for a freestanding Sn layer (i.e., a freestanding stanene layer) by theory (4.4×10^5 m/s)[5]. In order to experimentally clarify the nature of this band, we carried out additional measurements. First, photon-energy dependent ARPES data recorded with 21.2 eV, 16.9 eV, and 5.9 eV yield identical dispersions for the band B1 (see Supplementary Figure 6), which confirms the 2D nature of the band. Second, the momentum-resolved constant binding energy maps shown in Fig. 3c–e indicate that the linearly dispersing band B1 exhibits a hexagon shaped emission pattern for large binding energies of 0.8 eV from the crossing point, i.e., the band B1 adopts the symmetry of the Au(111) substrate. When approaching the Fermi energy, the pattern transforms to predominately a three-fold symmetric emission pattern. Third, we find that the band B1 possesses the same
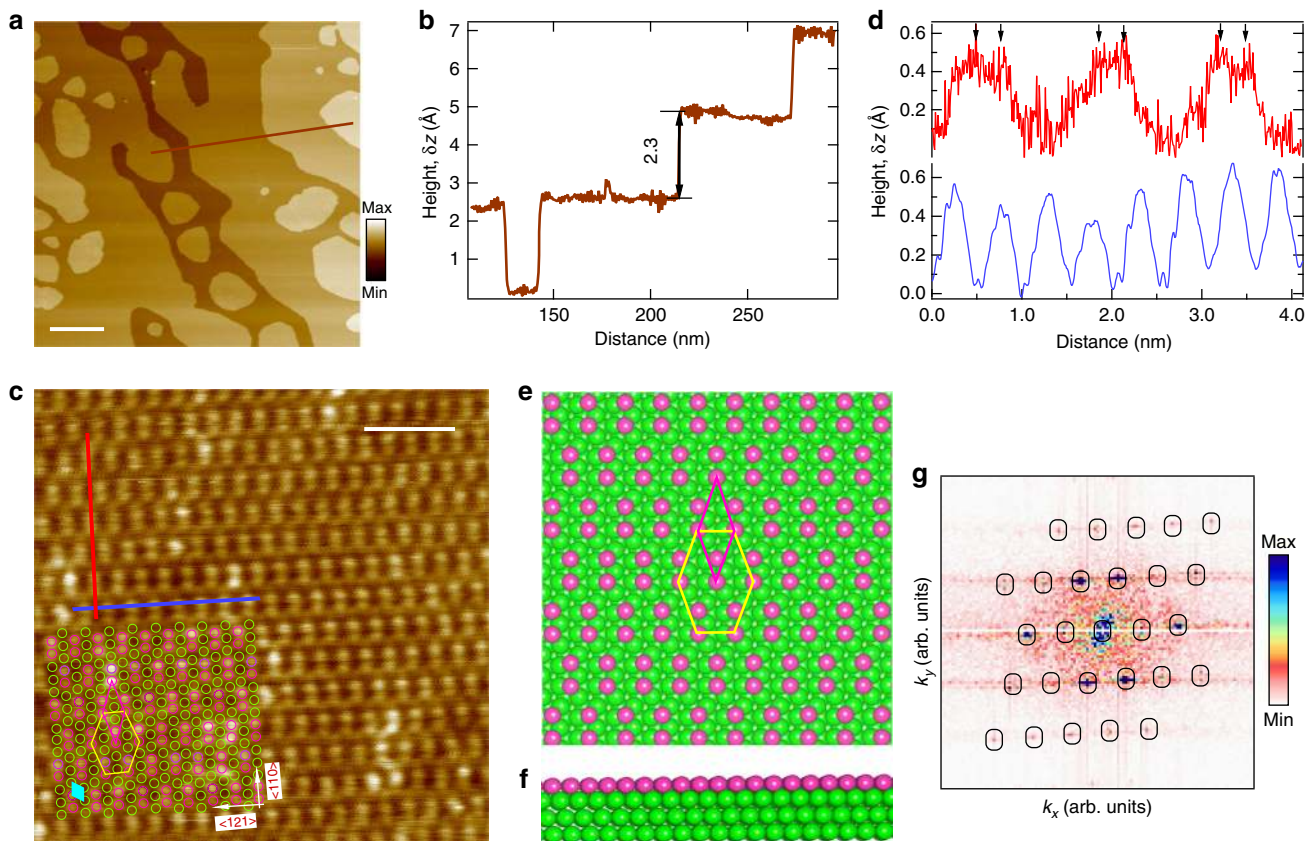
Fig. 2 Atomic structure of the $\sqrt{7}$ phase of Sn/Au(111). **a** The large area (300 nm × 300 nm, $U_{\text{Bias}} = 0.2$ V, $I_{\text{tunnel}} = 1.3$ nA) scanning tunneling microscopy (STM) image. The homogeneity of the STM data underlines the smooth and uniform growth of Sn on Au(111). The scale bar in **a** corresponds to 50 nm. **b** The exemplary height line profile extracted from **a** shows typical step height of 2.3 ± 0.2 Å. **c** The small area high-resolution STM image ($U_{\text{Bias}} = 0.01$ V, $I_{\text{tunnel}} = 8.9$ nA) shows the atomic structure of a single domain of the $\sqrt{7}$ phase of Sn/Au(111). The positions of the Sn atoms are well resolved and appear as white spots. The overlaid structural model shows the top layer of the face-centered cubic lattice of the substrate. The green and pink circles represent the Au atoms and the Sn adatoms, respectively. The stretched hexagon superstructure unit cell is shown as yellow hexagon. The primitive unit cells of the Sn adatom and of the substrate Au(111) are shown as pink and cyan diamonds, respectively. The scale bar in **c** corresponds to 2 nm. **d** Height line profiles extracted from **c** along the indicated directions marked with identical color. Small black arrows indicate the positions of the Sn atoms. Based on the experimental data, we propose a structural model for the $\sqrt{7}$ Sn/Au(111) phase shown in **e** (top view) and **f** (side view). The green and pink circles represent the Au and Sn atoms, respectively. **g** Fast Fourier transform (FFT) of high-resolution STM image shown in **c**. The FFT pattern agrees well the LEED pattern of a single domain of the $\sqrt{7}$ phase. The positions of the spots in FFT are highlighted by circles as guided to the eye. All data were recorded at room temperature

spectral intensity in whole momentum space ($k_{\|x}$, $k_{\|y}$ directions), pointing to conical-shaped band structure. Fourth, we carried out angle-resolved two-photon photoemission spectroscopy[26,27] to access the unoccupied part of the conical band B1, see Fig. 4a. In the unoccupied part of the spectrum, we indeed find bands that possibly extend band B1. However, the dispersion of these bands deviates from the linear behavior as seen in the occupied part of the spectrum. Instead, we find a nearly parabolic dispersion with the band bottom around the Fermi-level within our experimental uncertainty, see Fig. 4b. Although a different dispersion of the same band below and above the crossing point seems to be surprising at first glance, comparable deviations have already been reported for various 2D materials and topological insulators in literature[6,28–31].

It should be noted, however, that further investigations are required to unambiguously reveal the nature of the connection between the occupied band B1 and unoccupied band B1', i.e., the present results do not show conclusively if B1 and B1' reveal a crossing point at E_F or not.

In addition to the central linearly dispersing band (B1), we find a sideband (labeled as B2 in Fig. 3b) that also disperses linearly. The band B2 is nearly parallel to B1 around the $\bar{\Gamma}$ point with uniform energy and momentum separation of $\Delta E \sim 0.6$ eV and

$\Delta k_{\|} \sim 0.12$ Å^{-1}, respectively. However, in contrast to B1, B2 exhibits substantial intensity variations for different $k_{\|x}$, $k_{\|y}$ directions, see Supplementary Figure 7. Also, an analysis of the unoccupied regime of the band structure neither reveals an extension of B2 nor a hole-like parabolic band close to E_F connecting the occupied branches of B1 and B2. These observations are clear indications than B1 and B2 are not conventional (partially occupied) hole-like Rashba-split bands of the Sn/Au interface as for instance observed for the prototypical Rashba systems BiAg$_2$ and BiCu$_2$[32–34]. Instead, we conclude that B2 has a different, most likely bulk origin (see Supplementary Note 1 and Supplementary Figure 4).

To further unravel the nature of the interesting surface band B1 with linear dispersion below the Fermi-level, we have performed spin-resolved ARPES measurements. The data were acquired at different emission angles which are marked in Fig. 5a (yellow lines). The recorded spin polarization corresponds to an in-plane vertical spin component (P_y) that is parallel to y-axis as shown in Figs 5b, c. The individual spin resolved photoemission spectra are shown in Figs 5d, e for both $\pm k_{\|}$ directions. The experimentally obtained spin-polarization is shown in Fig. 5f. The spin polarization was calculated using $P = ((I^\uparrow - I^\downarrow)/(I^\uparrow + I^\downarrow))(1/S)$,
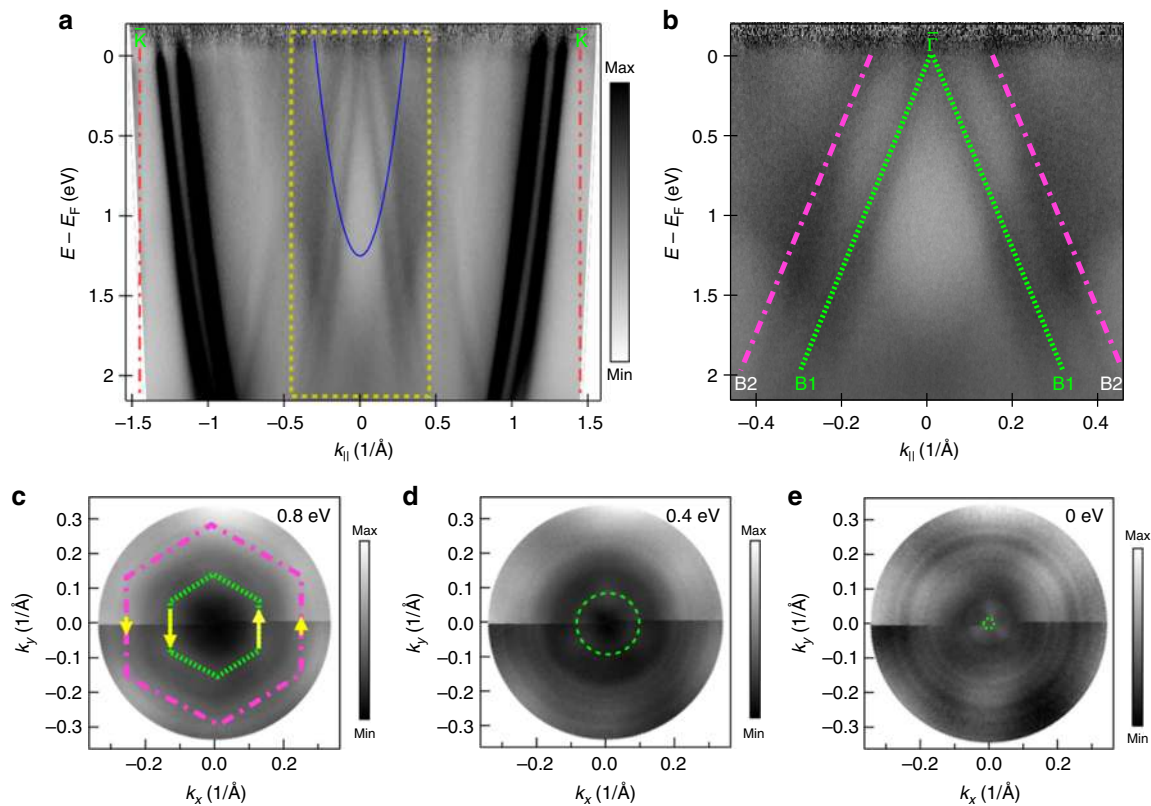
Fig. 3 Angle-resolved photoemission spectroscopy data imaging occupied electronic band structure around the $\bar{\Gamma}$-point. **a** Electronic structure of the $\sqrt{7}$ phase of Sn/Au(111) over a wide $E(k_{\|})$ range probed by angle-resolved photoemission spectroscopy (ARPES). The blue parabola marks the surface-projected L-band gap of the bulk Au(111). **b** An expanded view of the rectangular region marked in **a** that shows the linearly dispersing feature around the $\bar{\Gamma}$ point, labeled as B1 (green dotted lines). The label B2 marks the sideband, which is indicated by pink dotted-dashed lines. All lines are guides to eye. Both **a** and **b** ARPES images were obtained by normalizing each angular channel by the averaged energy-distribution curve obtained from the entire angular range of the corresponding image. **c–e** constant energy $k_{\|x} - k_{\|y}$ maps for different binding energies. The arrows in **c** depict the observed spin texture. All data were recorded at room temperature. Note the differences in the color scale

where $I^{\uparrow,\downarrow}$ are the ARPES intensities of two distinct spin polarization channels and S is the Sherman factor. The data shown in Fig. 5d–h are obtained by $N_{\uparrow,\downarrow} = I_t \ (1 \pm P)$, where $I_t = (I^{\uparrow} + I^{\downarrow})$. The first point we note is that the band B1 is indeed spin polarized with significant magnitude. As seen from Fig. 5f, the relative sign of the spin polarization is opposite to one another with respect to $\pm k_{\|}$ momentum direction, while the magnitude is almost identical. In other words, band B1 shows negative spin-polarization for positive momenta $(+k_{\|})$ and positive spin-polarization for negative momenta $(-k_{\|})$. The sideband B2 also shows a distinct spin-polarization with very small magnitude but identical sign as the band B1, see Fig. 5i. As presented in Supplementary Figure 8, the lack of visible dispersion of the bands B1 and B2 in the spin-resolved ARPES data is a direct consequence of the lower angular resolution of the spin-resolved ARPES experiment. However, when all spin-polarization curves of all four energy distribution curves (EDC) cuts are overlaid as shown in Supplementary Figure 8, we see that the spin-polarization curves clearly resemble the dispersion of the band B1.

We note that based on the presented data, we can only focus on the relative sign of the spin polarization of both bands B1 and B2. A more in-depth discussion of the absolute magnitude and sign of the spin-polarization of both bands would be too speculative due to the unknown contribution of final-state effects to the experimentally determined spin-resolved photoemission data. Nevertheless, spin textures in non-magnetic materials are typically induced by either Rashba-type spin-orbit splitting[26,35],

as for instance in Au(111)[36,37], or by a topological insulator phase, such as Bi_2Se_3[38] or α-Sn[19,20]. In case of a conventional Rashba splitting, however, the bands typically exhibit two parabolas with relatively opposite sign of spin polarization with respect to $\pm k_{\|}$ direction that are separated in momentum space by a constant k_0. This means that in the simplest case, one would expect four bands in total with alternating sign of their spin polarization, for instance up-down-up-down. Although this is in clear contrast to our experimental findings, it is not a conclusive proof of the absence of Rashba-type surface states at the Sn/Au interface.

Most remarkable, the spin polarization of band B1 resembles the spin-texture of a typical topological insulator phase, such as Bi_2Se_3. This seems to be surprising at first since the metallic substrate Au does not show a real band gap around E_F, but only a projected band gap. However, anti-symmetric spin polarizations of linear (Dirac-like) electronic states have already been reported for metallic surfaces and have been discussed in a very similar manner as topological insulators[39,40].

Discussion

Our extensive experimental study reveals interesting similarities between the Sn $\sqrt{7}$-superstructure of the Sn/Au(111) interface and elemental 2D graphene-like materials. For instance, the formation of a (stretched) honeycomb structure with a two-atomic basis are common structural fingerprints for the formation of a 2D graphene-like structure and have also been observed for the
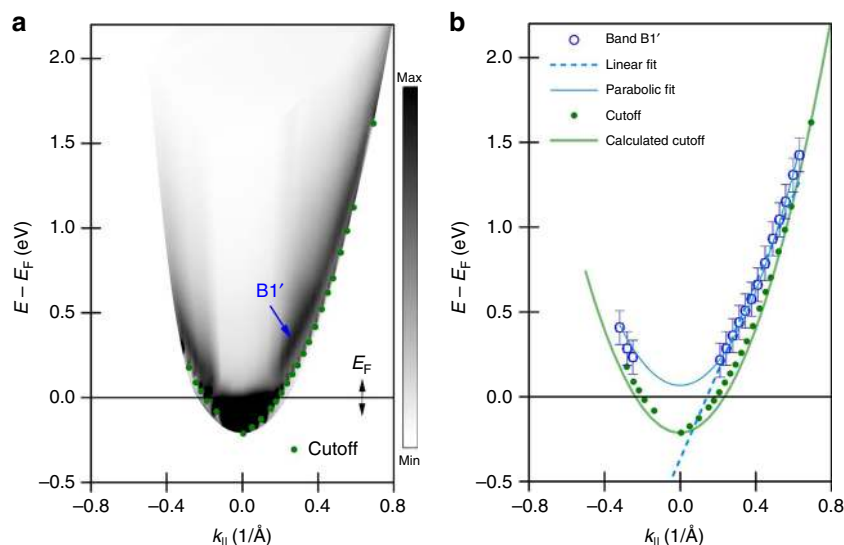
Fig. 4 Angle-resolved two-photon photoemission data imaging the unoccupied states of the $\sqrt{7}$ Sn/Au superstructure. **a** Angle-resolved two-photon photoemission (AR-2PPE) map recorded along the $\overline{\Gamma K}$ direction. A parabolic band is visible in the unoccupied part of the spectrum (B1′), which possibly reflects the spectroscopic signal of the extension of the nearly linear dispersing band B1 in the occupied part of the spectrum, as found in the conventional angle-resolved photoemission spectroscopy data presented in our work. The high intensity at small intermediate state energies and below the Fermi level (E_F) is caused by direct one-photon photoemission (which has very high transition probability compared to the second-order two-photon photoemission process) from the Au d-bands. The double-side-arrow at the Fermi level marks the uncertainty of the absolute energy scale due to space-charge effects, caused by the unavoidable high number of direct one-photon photoemitted electrons from the occupied states. **b** Extracted parabolic dispersion of the B1′ state (blue circle) and parabolic fit to the data (blue line). In addition, **b** shows a comparison of the theoretical cut-off of the photoemission cone (green line) with the experimentally observed cut-off (green points). This comparison was used to estimate the errors in our analysis of the state B1′ due to space-charge-induced momentum and energy spread in the spectrum

first experimental realization of the 2D Sn analog (stanene) on the topological insulator Bi_2Te_3[11]. Similarly, the electronic band structure reveals certain signatures that are expected for a 2D Dirac-material with strong spin-orbit coupling or a 3D topological insulator. The $\sqrt{7}$-phase shows a linearly dispersing band below the Fermi level with extremely high Fermi velocity and an alternating spin polarization. We attribute these intriguing findings to a strong lateral (chemical) bonding between the nearest neighbors Sn atoms within the Sn superstructure. The existence of such a strong in-plane interaction is also reflected in the structural properties of the Sn overlayer, in particular in the inhomogeneous distribution of the Sn atoms in the unit cell caused by the clustering of Sn atoms into Sn dimers.

However, there are also several features of the $\sqrt{7}$-phase that are decidedly different in comparison to the expectations for a 2D stanene sheet on a surface. First, the most surprising structural observation is the planar geometry of the $\sqrt{7}$ superstructure on Au(111), which is in clear contrast to the predicted vertical zigzag structure of freestanding stanene[5] or the vertical buckling of the Sn atoms on Bi_2Te_3[11]. Second, the dispersion of the linear band B1 changes significantly when crossing the Fermi energy from the occupied to the unoccupied part of the band structure. In addition, B1 appears at the $\overline{\Gamma}$ point rather than at the $\overline{K}$ point as expected for typical graphene analogs. We hence suspect that both observations are mediated by the interaction across the Sn-Au interface. In fact, it has been theoretically predicted that a certain interaction between Sn and the substrate is intrinsically required to stabilize the Sn superstructure on a metal surface[17]. The planar structure of the $\sqrt{7}$ phase might hence be stabilized by the saturation of the Sn π-orbitals by bonding to the Au substrate. This scenario closely corresponds to the chemical functionalization of stanene by halogens as discussed in Xu et al.[5]. Similarly, a strong hybridization across the Sn/Au interface naturally causes a strong alteration of the electronic properties of the Sn layer. For

example, and similarly to the recently proposed chemical functionalization of stanene[5], the hybridization can lead to a gap opening of Dirac bands at the $\overline{K}$ point, and the simultaneous appearance of a Dirac-like feature at the $\overline{\Gamma}$ point, as found here.

Altogether, our experimental findings strongly suggest that the extraordinary properties of the $\sqrt{7}$ phase, i.e., the stretched honeycomb-like structure, the linearly dispersing band below the Fermi level with extremely high Fermi velocity and an alternating spin polarization, are determined by a delicate balance between the interaction of the Sn overlayer with the Au substrate as well as by the intrinsic properties and interatomic interactions of the atomically thin Sn film.

In conclusion, our experimental observation lays the foundation to fabricate and investigate a new 2D allotrope of the Sn on Au(111) surface with exotic spin-dependent electronic properties. The band structure of this superstructure is dominated by a linearly dispersing band centered at the $\overline{\Gamma}$ point with an exceptionally high Fermi velocity of $v_F \approx 1 \times 10^6$ m/s and the spin-texture of a three-dimensional topological insulator. These exceptional properties of the 2D Sn/Au interface are the result of a hybridization of electronic states of the Sn orbitals with bands of the Au(111) surface as well as of a direct chemical interaction between neighboring Sn atoms in the overlayer leading to the formation of stretched honeycomb structure of Sn dimers.

We propose that the introduced Sn/Au interface system is a highly interesting case study that proves the tunability of atomically thin 2D materials by adsorption on metallic surfaces[41], in line with recent progress in the exploitation of interfacial effects with carbon-based overlayers in the field of molecular spin-tronics[42]. To take advantage of the exceptional electronic properties of this novel 2D allotrope of Sn on Au(111) in a device structure, we envision to severely reduce the thickness of the Au substrate down to a few or even a single monolayer. In this way, quantum-confinement[26,27,43–45] can be used to tune and reduce
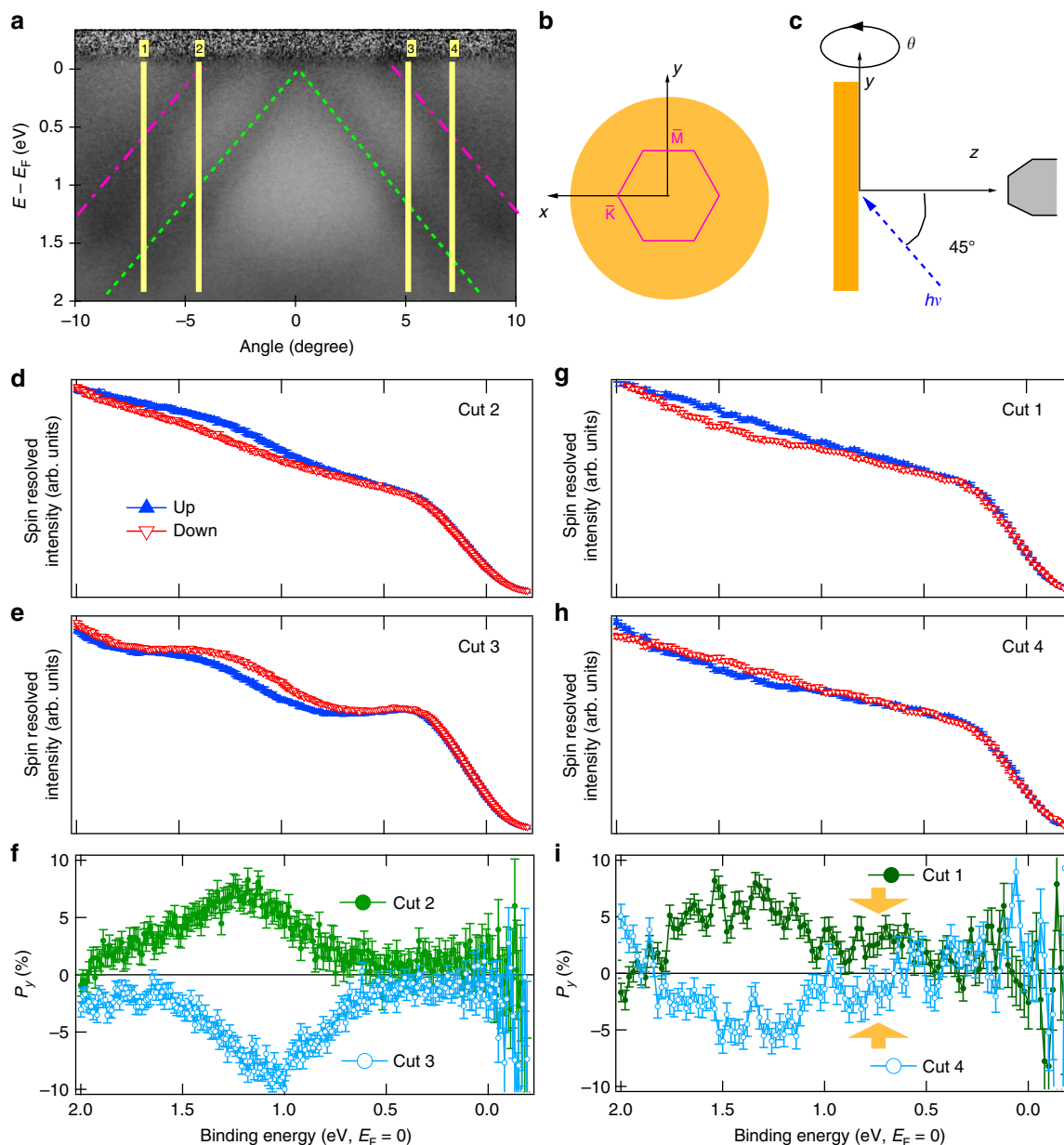
Fig. 5 Spin texture of the $\sqrt{7}$ phase of Sn/Au(111). **a** Angle-resolved photoemission spectroscopy (ARPES) data showing the momentum space positions of the spin-resolved energy-distribution curves (**d**, **e**, **g**, **h**) at four selected emission angles, as indicated by the yellow vertical lines labeled 1 to 4. **b** A schematic illustration of the coordinate system of the sample in normal emission geometry. **c** The geometry of the non-polarized monochromatized He I_α vacuum ultraviolet light source used for our photoemission experiment with respect to the sample surface and the electron analyzer. The incoming radiation is located the y–z plane. Angle-dependent photoemission spectra were obtained by rotating (polar angle) the sample around the y-axis. The spin-resolved ARPES intensity corresponds to the in-plane vertical (P_y) spin component. The green dotted lines and pink dotted-dashed lines mark the B1 and B2 band, respectively. **f** and **i** spin polarization obtained from **d**, **e** and **g**, **h**. In **h**, the energy position of the B2 band is indicated by arrows and the broad peak centered at around 1.4 eV originates from the B1 band. Since the spin polarization of the band B2 is very small in magnitude and might even originate from the overlap with B1, we will not further discuss this band. The error bar in **f** and **i** corresponds to the standard deviation of the respective measurements. The relatively low spin polarization is consequence of having just a single layer of Sn superstructure on Au(111). All data were recorded at room temperature

the available Au electronic states at the Fermi-surface, which might lead to a scenario where the dominant charge and spin transport is mediated by electronic states of the Sn-based 2D superstructure.

Methods

Spin- and angle-resolved photoemission measurements. The experiments were conducted in multiple ultra-high vacuum chambers with base pressure better than 1×10^{-10} mbar. The angle-resolved photoemission spectroscopy (ARPES)

measurement was carried out using a monochromatized non-polarized ultraviolet light source (21.22 eV) and a 2D hemispherical electron energy analyzer. The spin-resolved photoemission measurements were performed using a combination of a 2D hemispherical electron energy analyzer for energy-filtering and a spin detector based on very low energy electron diffraction (VLEED) from an oxygen-passivated epitaxial Fe film on W(100). The spin polarization was calculated by using the calculated Sherman factor of the used VLEED detector ($S = 0.29$). The energy and angular resolution were set to better than 30 meV and 0.3°, respectively. In order to construct the $k_{\|x} - k_{\|y}$ ARPES map, the data were acquired by continuously changing the azimuth orientation of the sample from 0° to 180° in steps of 1°, while keeping the polar angle constant. Thereafter, the constant energy $k_{\|x} - k_{\|y}$ map

was extracted from the 3D data cube by selecting a particular binding energy slice of the data cube and averaging the intensity over an energy window of ±25 meV around the central binding energy. The total energy (angular) resolution for ARPES and spin-resolved ARPES measurements are better than 100 meV (0.3°) and 250 meV (± 1.5°), respectively. All experiments were conducted at room temperature.

Angle-resolved two photon photoemission measurement. The angle-resolved two photon photoemission (AR-2PPE) experiment was carried out at room temperature using a photon energy of 4.8 eV generated from a frequency-quadrupled fiber laser system. The measurement was carried out with 6.5 V sample bias, so that electrons with very low kinetic energy of <1 eV can still be measured. The distortions of the photoemission distribution introduced by the sample bias were corrected with the model described in Hengsberger et al.[46].

Scanning tunneling microscopy experiments. All scanning tunneling microscopy (STM) data were acquired at room temperature using the constant current mode. The STM images presented in this work were processed with the Nanotec Electronica WSxM[47] and the Gwyddion software[48].

Sample preparation. The Au(111) sample was cleaned by cycles of Ar-ion sputtering, followed by sample annealing at around 800 K. The cleanliness of the surface was confirmed by the presence of a sharp $(22 \times \sqrt{3})$ low energy electron diffraction (LEED) pattern of the herringbone reconstruction and the clearly resolved spin-split surface state in angle-resolved photoemission spectroscopy (ARPES). High purity Sn (99.9999%) was evaporated from a homemade water-cooled Knudsen type thermal evaporator, using a paralytic boron nitrate (PBN) crucible at about 1150 K. During the deposition, the chamber pressure always stayed below $2-5 \times 10^{-10}$ mbar. The Sn coverage was calibrated by defining that 0.3 monolayer (ML) of Sn are necessary to form a $(\sqrt{3} \times \sqrt{3})$R30° structure of Sn/Au (111). The Sn coverage for subsequent depositions was interpolated with the assumption of a coverage-independent sticking coefficient for Sn on Au(111). All Sn-depositions and measurements were carried out at room temperature.

Code availability. All relevant code used for data analysis are available upon reasonable request.

Data availability
All relevant data are available from the authors upon reasonable request.

References
1. Novoselov, K. S. et al. Electric field effect in atomically thin carbon films. *Science* **306**, 666 (2004).
2. Geim, A. K. Graphene: status and prospects. *Science* **324**, 1530 (2009).
3. Molle, A. et al. Buckled two-dimensional Xene sheets. *Nat. Mater.* **16**, 163 (2017).
4. Balendhran, S., Walia, S., Nili, H., Sriram, S. & Bhaskaran, M. Elemental analogues of graphene: silicene, germanene, stanene, and phosphorene. *Small* **11**, 640–652 (2015).
5. Xu, Y. et al. Large-gap quantum spin Hall insulators in tin films. *Phys. Rev. Lett.* **111**, 136804 (2013).
6. Tang, P. et al. Stable two-dimensional dumbbell stanene: a quantum spin Hall insulator. *Phys. Rev. B* **90**, 121408 (2014).
7. Wu, S.-C., Shan, G. & Yan, B. Prediction of near-room-temperature quantum anomalous Hall effect on honeycomb materials. *Phys. Rev. Lett.* **113**, 256401 (2014).
8. Wang, J., Xu, Y. & Zhang, S.-C. Two-dimensional time-reversal-invariant topological superconductivity in a doped quantum spin-Hall insulator. *Phys. Rev. B* **90**, 054503 (2014).
9. Xu, Y., Gan, Z. & Zhang, S.-C. Enhanced thermoelectric performance and anomalous seebeck effects in topological insulators. *Phys. Rev. Lett.* **112**, 226801 (2014).
10. Rivero, P., Yan, J.-A., García-Suárez, V. M., Ferrer, J. & Barraza-Lopez, S. Stability and properties of high-buckled two-dimensional tin and lead. *Phys. Rev. B* **90**, 241408 (2014).
11. Zhu, F. et al. Epitaxial growth of two-dimensional stanene. *Nat. Mater.* **14**, 1020 (2015).
12. Deng, J. et al. Epitaxial growth of ultraflat stanene with topological band inversion. *Nat. Mater.* **17**, 1081–1086 (2018).
13. Xu, Y., Tang, P. & Zhang, S.-C. Large-gap quantum spin Hall states in decorated stanene grown on a substrate. *Phys. Rev. B* **92**, 081112 (2015).
14. Fang, Y. et al. Quantum spin Hall states in stanene/Ge(111). *Sci. Rep.* **5**, 14196 (2015).
15. Suarez Negreira, A., Vandenberghe, W. G. & Fischetti, M. V. *Ab initio* study of the electronic properties and thermodynamic stability of supported and functionalized two-dimensional Sn films. *Phys. Rev. B* **91**, 245103 (2015).
16. Wang, H. et al. Possibility of realizing quantum spin Hall effect at room temperature in stanene/Al$_2$O$_3$(0001). *Phys. Rev. B* **94**, 035112 (2016).
17. Nigam, S., Gupta, S., Banyai, D., Pandey, R. & Majumder, C. Evidence of a graphene-like Sn-sheet on a Au(111) substrate: electronic structure and transport properties from first principles calculations. *Phys. Chem. Chem. Phys.* **17**, 6705 (2015).
18. Fu, L. & Kane, C. L. Topological insulators with inversion symmetry. *Phys. Rev. B* **76**, 045302 (2007).
19. Barfuss, A. et al. Elemental topological insulator with tunable Fermi level: Strained α-Sn on InSb(001). *Phys. Rev. Lett.* **111**, 157205 (2013).
20. Ohtsubo, Y., Le Fevre, P., Bertran, Francois & Taleb-Ibrahimi, A. Dirac cone with helical spin polarization in ultrathin α-Sn(001) films. *Phys. Rev. Lett.* **111**, 216401 (2013).
21. Yan, B. et al. Topological states on the gold surface. *Nat. Commun.* **6**, 10167 (2015).
22. Barthès, M.-G. & Pariset, C. A low energy electron diffraction-Auger electron spectroscopy study of alloy formation during the adsorption of tin on (100) and (111) Au. *Thin. Solid. Films.* **77**, 305 (1981).
23. Maniraj, M. et al. Structure and electronic properties of the $(\sqrt{3} \times \sqrt{3})$R30° SnAu$_2$/Au(111) surface alloy. *Phys. Rev. B* **98**, 205419 (2018).
24. Novoselov, K. S. et al. Two-dimensional gas of massless Dirac fermions in graphene. *Nature* **438**, 197 (2005).
25. Castro Neto, A. H., Guinea, F., Peres, N. M. R., Novoselov, K. S. & Geim, A. K. The electronic properties of graphene. *Rev. Mod. Phys.* **81**, 109 (2009).
26. Mathias, S. et al. Quantum-well-induced giant spin-orbit splitting. *Phys. Rev. Lett.* **104**, 066802 (2010).
27. Mathias, S. et al. Band structure dependence of hot-electron lifetimes in a Pb/Cu(111) quantum-well system. *Phys. Rev. B* **81**, 155429 (2010).
28. Guo, Y. et al. Interfacial properties of stanene–metal contacts. *2D Mater.* **3**, 035020 (2016).
29. Scholz, M. R. et al. Tolerance of topological surface states towards magnetic moments: Fe on Bi$_2$Se$_3$. *Phys. Rev. Lett.* **108**, 256810 (2012).
30. Wang, Y. H. et al. Measurement of intrinsic Dirac Fermion cooling on the surface of the topological insulator Bi$_2$Se$_3$ using time-resolved and angle-resolved photoemission spectroscopy. *Phys. Rev. Lett.* **109**, 127401 (2012).
31. Xu, C.-Z. et al. Elemental topological Dirac semimetal: α-Sn on InSb(111). *Phys. Rev. Lett.* **118**, 146402 (2017).
32. Ast, C. R. et al. Giant spin splitting through surface alloying. *Phys. Rev. Lett.* **98**, 186807 (2007).
33. Bentmann, H. et al. Spin orientation and sign of the Rashba splitting in Bi/Cu (111). *Phys. Rev. B* **84**, 115426 (2011).
34. Noguchi, R. et al. Direct mapping of spin and orbital entangled wave functions under interband spin-orbit coupling of giant Rashba spin-split surface states. *Phys. Rev. B* **95**, 041111 (2017).
35. Dil, J. H. Spin and angle resolved photoemission on non-magnetic low-dimensional systems. *J. Phys. Condens. Matter* **21**, 403001 (2009).
36. LaShell, S., McDougall, B. A. & Jensen, E. Spin splitting of an Au(111) surface state band observed with angle resolved photoelectron spectroscopy. *Phys. Rev. Lett.* **77**, 3419 (1996).
37. Hoesch, M. et al. Spin structure of the Shockley surface state on Au(111). *Phys. Rev. B* **69**, 241401 (2004).
38. Jozwiak, C. et al. Photoelectron spin-flipping and texture manipulation in a topological insulator. *Nat. Phys.* **9**, 293 (2013).
39. Miyamoto, K. et al. Spin-polarized Dirac-cone-like surface state with *d* character at W(110). *Phys. Rev. Lett.* **108**, 066808 (2012).
40. Kutnyakhov, D. et al. Spin texture of time-reversal symmetry invariant surface states on W(110). *Sci. Rep.* **6**, srep29394 (2016).
41. Kim, K. S., Jung, S. C., Kang, M. H. & Yeom, H. W. Nearly massless electrons in the silicon interface with a metal film. *Phys. Rev. Lett.* **104**, 246803 (2010).
42. Cinchetti, M., Dediu, V. A. & Hueso, L. E. Activating the molecular spinterface. *Nat. Mater.* **16**, 507–515 (2017).
43. Bian, G., Zhang, L., Liu, Y., Miller, T. & Chiang, T.-C. Illuminating the surface spin texture of the Giant-Rashba quantum-well system Bi/Ag(111) by circularly polarized photoemission. *Phys. Rev. Lett.* **108**, 186403 (2012).
44. Cercellier, H. et al. Spin-orbit splitting of the Shockley state in the Ag/Au(111) interface. *Phys. Rev. B* **70**, 193412 (2004).
45. Cercellier, H. et al. Interplay between structural, chemical, andau spectroscopic properties of Ag/Au(111) epitaxial ultrathin films: A way to tune the Rashba coupling. *Phys. Rev. B* **73**, 195413 (2006).
46. Hengsberger, M., Baumberger, F., Neff, H. J., Greber, T. & Osterwalder, J. Photoemission momentum mapping and wave function analysis of surface and bulk states on flat Cu(111) and stepped Cu(443) surfaces: A two-photon photoemission study. *Phys. Rev. B* **77**, 085425 (2008).

47. Horcas, I. et al. WSXM: A software for scanning probe microscopy and a tool for nanotechnology. *Rev. Sci. Instrum.* **78**, 013705 (2007).
48. Nečas, D. & Klapetek, P. Gwyddion: an open-source software for SPM data analysis. *Open Phys.* **10**, 181–188 (2011).

Author contributions
The experiments were conceived, planned, and supervised by M.M., B.S., M.C., S.M., and M.A. M.M. established the phase diagram based on the LEED measurement and iden-tified the stanene-like phase using ARPES. M.M., D.J., S.E., and S.J. performed the ARPES using different light sources. M.M., D.J., J.S., and A.J. performed the spin-resolved ARPES experiments. M.M., L.L., J.K., and Z.W. performed the STM measure-ment. M.D. and S.S. performed the two-photon-photoemission experiments. W.S. and B. Y. contributed to the discussion of the experimental data in the light of state-of-the-art theory in the field of topological materials. The data were analyzed by all authors. All authors discussed the results and contributed to the final manuscript.

Additional information
Supplementary information accompanies this paper at https://doi.org/10.1038/s42005-019-0111-2.

Competing interests: The authors declare no competing interests.

Reprints and permission information is available online at http://npg.nature.com/reprintsandpermissions/

Publisher's note: Springer Nature remains neutral with regard to jurisdictional claims in published maps and institutional affiliations.